Research Article | Vol. 17, No. 7 / 1 Jul 2026 / Biomedical Optics Express 3854
Biomedical Optics EXPRESS

Hadamard-encoded scattered light imaging for faster, signal-enhanced mapping of brain fiber orientations

DENNIS SCHEIDT,[1,*] FELIX MATUSCHKE,[1] KATRIN AMUNTS,[1,2] MIRIAM MENZEL,[1,3,†] AND MARKUS AXER[1,4,†]

[1] *Institute of Neuroscience and Medicine (INM-1), Forschungszentrum Jülich GmbH, Wllhelm-Johnen-Straße, Jülich 52425, Germany*
[2] *C. & O. Institute of Brain Research, Heinrich-Heine University Düsseldorf, Merowinger Platz 1a, Düsseldorf, Germany*
[3] *Department of Imaging Physics, Delft University of Technology, Lorentzweg 1, Delft 2628 CJ, The Netherlands*
[4] *School of Mathematics and Natural Sciences, University of Wuppertal, Gaussstraße, Wuppertal, Germany*
[†] These authors contributed equally
[*] *d.scheidt@fz-juelich.de*

Abstract: A deeper understanding of brain function requires resolving the intricate networks formed by neurons at the microscopic scale. Imaging the connecting nerve fibers remains a significant challenge, particularly due to the difficulty of resolving crossing fibers using conventional optical imaging techniques. Computational Scattered Light Imaging (ComSLI) addresses this by using obliquely incident light to reconstruct the in-plane orientations of nerve fibers based on their scattering profiles, enabling the resolution of fiber crossings. One approach is to use an LED display as a light source, which allows for illuminating the sample by arbitrary patterns and measuring full scattering patterns as well as angular scattering profiles. However, when using an LED display instead of a high-intensity LED spot, ComSLI is limited by a low signal and acquisition times of several seconds per image. To overcome these limitations, this work introduces Hadamard basis sampling for the angular illumination patterns, allowing an increase in illumination intensity and a corresponding reduction in measurement time. Compared to standard sampling approaches, this method yields significantly sharper defined scattering peaks, resulting in enhanced angular resolution of the scattering profiles. The Hadamard-based illumination enhances the reconstruction of cortical fiber organization, overcoming a key limitation in challenging ComSLI applications and neuroscience.

1. Introduction

One of the major current challenges in neuroscience is understanding the functionality of the human brain. A key step toward this goal is to unravel the neuronal anatomical architecture at the (sub-)cellular level. A human brain contains 86 billions of neurons, each forming up to several thousand connections with other neurons, resulting in a highly complex, multilayered network [1,2].

Optical microscopy provides resolution at the (sub-)micrometer scale and is thus widely used to image cellular structures. Histological staining is commonly employed to visualize neuronal cells or myelinated or non-myelinated axons (in the following referred to as "nerve fibers") under bright-field microscopy. However, it requires distinct protocols to highlight specific structures and involves extensive manual sample preparation [3,4]. While staining can reveal the presence and location of nerve fibers, it does not provide directional information, necessitating additional image processing to infer fiber orientations similar to what is known from diffusion magnetic resonance imaging (dMRI) techniques though at much larger scales [5].

#596576 https://doi.org/10.1364/BOE.596576
Journal © 2026 Received 11 Mar 2026; revised 28 May 2026; accepted 14 Jun 2026; published 25 Jun 2026

Biomedical Optics EXPRESS

Label-free imaging techniques such as 3D Polarized Light Imaging (3D-PLI) or Computational Scattered Light Imaging (ComSLI) offer alternatives that do not require staining and are sensitive to specific birefringent or anisotropic tissue components such as nerve fibers. 3D-PLI uses optical birefringence and tilted illumination paths to extract the 3D orientation of nerve fibers [6].

ComSLI is a recently developed microscopy technique that exploits the anisotropic scattering properties of nerve fibers (or other fibrous structures) to infer their orientation within the image or sample plane [7]. While the out-of plane orientation is also contained in the signal [8], a theory to quantitatively assess the inclination angle is currently under development. The working principle is conceptually similar to X-ray crystallography, in which the spatial scattering pattern of a sample is recorded to infer its geometrical properties [9]. In ComSLI, the optical path is inverted to suit microscopy: the sample is illuminated at a fixed polar angle from different azimuthal directions, and the camera captures the scattered light. In this configuration, the scattering angle θ corresponds to the polar angle of the oblique illumination.

Azimuthal illumination positions are typically implemented using a rotating LED-spot [10], effectively functioning as point light source. Alternatively, azimuthal angles can be sampled by projecting ring segments onto an LED panel or display, generating the desired illumination patterns [7,11,12]. By acquiring one image per azimuthal direction, angular scattering profiles are recorded for each pixel in the field of view. The fiber orientation is then inferred from the locations of the scattering peaks. A key advantage of this approach is its ability to resolve fiber crossings, as multiple scattering peak pairs correspond to multiple in-plane fiber orientations. These fiber orientation maps are potentially usable in the future for tractography algorithms, such as known from dMRI applications, to reconstruct fiber pathways at the microscopic scale [13,14].

One of the main challenges in ComSLI is the low scattered light intensity caused by oblique illumination, which results in long acquisition times and low signal-to-noise ratio (SNR), especially in highly heterogeneous regions such as the cerebral cortex, which is rich in neurons and other cellular and vascular structures and contains sparsely distributed fibers with diverse orientations. Furthermore, standard LED rings or displays have significantly lower brightness compared to high-power LED-spots, further limiting achievable SNR. However, in contrast to LED-spots, LED displays allow the additional acquisition of full scattering patterns and dynamic changes to the angular scattering patterns, by varying the radius and angular resolution of the displayed patterns.

Single-Pixel Imaging (SPI) is based on the principle that the intensity of an incoherent light field can be decomposed into a series of spatial modes. By sampling the field with a Spatial Light Modulator (SLM) or Digital Micromirror Device (DMD) and projecting it onto a single large detector – typically a photodiode – the spatial distribution of the light field, or image, can be reconstructed [15,16]. Because SPI activates multiple spatial modes during the measurement of a single basis element, each sampled element contains redundant information from the canonical basis elements. This redundancy enables compressive sensing reconstruction algorithms to reduce the number of illuminations or images required per measurement [17]. In this article, Hadamard basis sampling in ComSLI is explored as a step toward compressive sensing in future applications.

Since ComSLI constructs an angular scattering profile per pixel from sequential measurements, the angular acquisition process can be represented as sampling in a canonical basis. SPI concepts can be extended to this framework: using Hadamard basis functions, which activate 50% of the optical elements at once, increases the total illumination intensity compared to the single-element canonical basis [18,19].

This work applies the Hadamard basis to sample the angular scattering profiles in ComSLI, using circular illumination patterns based on the annular Hadamard basis sampling implementation described in [20], and compares the results with the previous canonical measurement strategy used in ComSLI [11,21]. Instead of illuminating from one angle at a time, the sample is illuminated

Biomedical Optics EXPRESS

from multiple azimuthal directions simultaneously, thus increasing the total illumination intensity and reducing the measurement time. The resulting angular scattering patterns are compared to those obtained from conventional ComSLI measurements with single-angle illumination, for both macroscopic Polyactide (PLA) samples and microscopic structures in human brain tissue.

The obtained angular scattering profiles and from these derived direction maps are compared, with particular attention to cortical regions of the brain, where sparsely distributed fibers are expected to exhibit grid-like crossings, as known from myeloarchitectonic research [22].

Compared with conventional canonical basis sampling used in previous ComSLI measurements, Hadamard basis sampling enables a tenfold reduction in camera exposure time for $N = 32$ basis elements. This reduction is important for high-throughput measurements of large whole-brain sections, where measurement time accumulates rapidly, and for fresh, unmounted samples, where biochemical processes can quickly alter the tissue. In addition, the illumination power increases by a factor of $N/2$, resulting in narrower scattering peaks compared with the canonical basis. Narrower peaks improve angular resolution and enhance the reconstruction of fibers with small crossing angles because neighboring scattering peaks can be distinguished more easily. This enables more accurate mapping of fiber orientations. Finally, the successful application of Hadamard basis sampling paves the way for compressive sensing of angular scattering profiles because the measurement basis contains redundant information. This may potentially reduce data storage requirements by $5 - 20\,\%$, which is particularly important for high-throughput measurements.

2. Methods

2.1. Experimental setup

The experimental setup is shown in Fig. 1(A) and has been described in [11]. In addition to ComSLI, it allows to perform Mueller polarimetry measurements and provides the possibility of correlative scattered and polarized light imaging measurements. For this purpose, variable liquid crystal retarders and linear polarizers were placed in the optical path. Since this work focuses on the scattered light imaging application, these elements were set to not obstruct or interfere with the scattered light and are therefore not shown in the experimental setup.

ComSLI samples the scattering patterns of a sample in an inverted manner compared to typical scattering experiments (see Fig. 1(A)) and thus requires oblique illumination of the sample from light from different azimuthal angles. For this purpose, a large-area light source with separately controllable LEDs (INFILED s1.8 LE Indoor LED Cabinet, operated at a frame rate of 2400 Hz) was used. The setup in Fig. 1(B) illustrates such an oblique illumination path. The LED display consists of 256×256 RGB LEDs, with a pitch of 1.8 mm and a viewing angle of 120°, spanning a total area of $46.56 \times 46.56\,\mathrm{cm}^2$. The maximum brightness of the panel is 1000 cd/m^2. The samples were placed 16 cm above the LED display, corresponding to the camera objective's focal distance.

The samples were imaged with a QIOPTIQ APO-RODAGON-D 1X 75/4,0 objective lens, which was placed at a distance of 16 cm above the sample holder, onto a Basler acA5472-17uc CMOS camera (Sony IMX183 CMOS sensor with a size of $13.1 \times 8.8\,\mathrm{mm}^2$, a sensor pixel size of $2.4 \times 2.4\,\mu\mathrm{m}^2$ and 5472×3648 pixels). This configuration yields a field of view of $8 \times 5\,\mathrm{mm}^2$, a pixel size in object space of approximately 1.5 µm, and an optical resolution of 2.19 µm, determined using a United States Air Force (USAF) resolution chart. To maximize light collection, the camera aperture was fully opened to its maximum setting of 5.6 mm.

The LED display was used to display the illumination patterns (ring segments) used for the ComSLI measurements. The basis is a centered ring with inner and outer radii of 50 and 90 LEDs, respectively, so that the area of the ring and thus the light intensity is maximized. This results in a polar illumination angle, i.e. scattering angle, of $\theta \approx 45°$. The ring is then divided into N azimuthal segments, corresponding to angular segment steps of $360°/N$ which determine the

Biomedical Optics EXPRESS

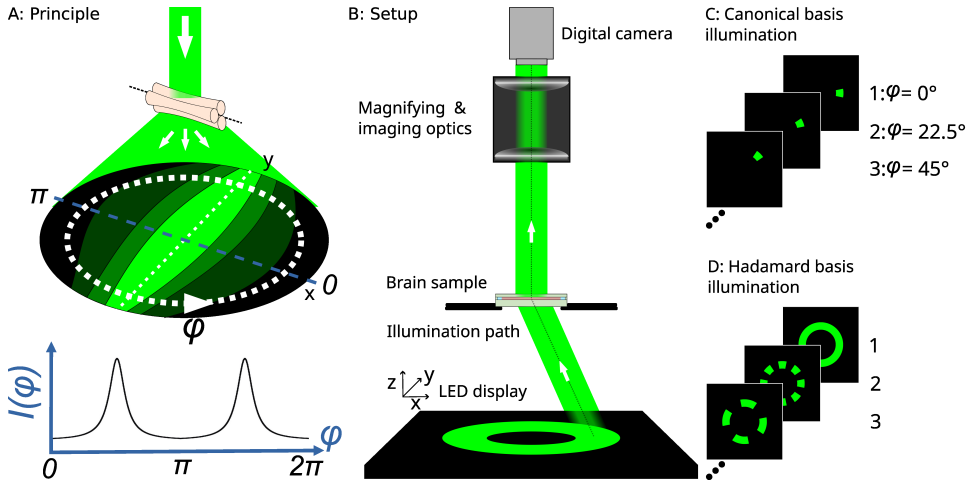

Fig. 1. Experimental setup. A: Principle of ComSLI. Normally incident light on an in-plane fiber bundle results in a symmetric scattering pattern, where the peaks in the azimuthal intensity profile $I(\varphi)$ are orthogonal to the in-plane orientation of the fibers. B: An LED display is used to display the light patterns for oblique illumination. Only the normally scattered (transmitted) light is measured by the digital camera. The illumination path demonstrates the illumination direction for $\varphi = 0°$. C and D: Three first illumination patterns of the canonical and Hadamard measurement basis, respectively.

azimuthal resolution of the scattering patterns. These ring segments form the basis elements that are used to implement the canonical and Hadamard bases. Although the LED display supports RGB illumination, only the green LEDs were used for the illumination patterns (see Fig. 1(C), (D)) to allow direct comparison with previous ComSLI studies using green light [11].

The exposure time t_{exp} for measurements with the canonical basis was 5 seconds, while the exposure time for the Hadamard basis was 0.5 seconds. It was chosen to avoid overexposure while ensuring a sufficient signal-to-noise ratio. No gain was used and only the green camera channel was evaluated. Because the red and blue pixel values are interpolated when generating a grayscale image, only the green pixels were used for data evaluation. All images were measured four times and averaged. The camera sensor uses a color filter array in which individual pixels capture different color channels. Angular ComSLI measurements were conducted for $N = 16, 32$ and 64 angular segments, resulting in a respective angular resolution of $[22.5, 11.25, 5.63]°$ while maintaining the initial exposure time for each basis. During a measurement, the different basis elements were displayed sequentially by synchronizing them internally with the camera trigger of the acquisition software. An external trigger was not necessary as the frame rate of the LED display (2400 Hz) is several orders of magnitude larger than the acquisition rate of the camera (canonical: 0.2 Hz, Hadamard: 2 Hz). The samples were measured first with the canonical basis and afterwards with the Hadamard basis without moving the sample, making the requirement of registration unnecessary.

By evaluating a homogeneous opal-glass scatterer (Edmund Optics #46-168), the optical scattering power was estimated for the different illumination bases according to [23]:

$$P_{\text{scat}} = \frac{S_{\text{img}}\ (e^-/DN)\ hc}{t_{\text{exp}}\ \eta\lambda},$$

where S_{img} is the total amount of counts of the acquired image, e^-/DN is the number of electrons per dynamic gray level in the camera, h is Planck's constant, c is the light speed and η is the

Biomedical Optics EXPRESS

quantum efficiency of the camera. For $N = 32$, the canonical basis yielded an optical scattering power of $P^{\mathrm{can}}_{N=32} = 13\,\mathrm{pW}$, whereas the initial Hadamard element, corresponding to full-ring illumination ($i = 0$), yielded $P^{\mathrm{Had}}_{i=0} = 430\,\mathrm{pW}$. The subsequent Hadamard elements yielded $P^{\mathrm{Had}}_{N=32} = 215\,\mathrm{pW}$. This is consistent with the expected scaling of the illuminated area, since the area of each canonical basis element decreases with $1/N$, whereas each Hadamard basis element activates 50% of the annular segments. Thus, for all Hadamard elements except the initial full-ring illumination, the optical power increases by a factor of

$$\frac{P^{\mathrm{Had}}_{N}}{P^{\mathrm{can}}_{N}} = \frac{N}{2}\,. \tag{1}$$

In standard ComSLI measurements, the sample is illuminated from a single direction. In the case of the Hadamard basis, the sample is illuminated from different directions at the same time. The implementation of such an illumination pattern is treated in Section 2.3.

2.2. Sample preparation

Three different samples were used for the scattering measurements. First, a remnant of hot PLA from a 3D printer was stretched along an objective holder to create rounded shapes simulating large fiber bundles with a thickness of $10 - 100\,\mu\mathrm{m}$. Subsequently, the PLA was covered in a 20% glycerol-water solution to mimic the preparation procedure of the brain tissue samples.

Second, a sample with known crossing of nerve fibers was studied. For this purpose, two sections of a human optic tract were placed on top of each other under a defined crossing angle. The sample was obtained from a brain (female, 74 years old) that was removed from the skull within 24 hours after death, fixed in a buffered solution of 4% formaldehyde for several weeks, immersed in a 20% glycerol-water solution, and deeply frozen. The optic chiasm was removed and cut along the fiber tracts of the visual pathway into 30 µm-thin sections with a cryostat microtome. One section was split at the median line and the sections of the optic tracts were manually placed on top of each other under a crossing angle of $50 - 60°$. The sample was mounted in a 20% glycerol-water solution and cover-slipped. See [24] for more details.

Third, a section of a human brain encompassing the cortical Broca region was investigated. The post-mortem brain sample (female, 80 years old) was formalin-fixed and deep-frozen as described above. The frozen brain was cut into 60 µm-thin sections which were mounted in a 20% glycerol-water solution in between coverslips. One section was selected for this study (see Supplement 1 Fig. S8). Detailed preparation protocols are described in [25].

This study was conducted in accordance with all applicable ethical regulations. All body donors provided written informed consent for the general use of post-mortem tissue for research and educational purposes. The use of the brain from which the optic tract sample was obtained, was approved by the Netherlands Brain Bank (ethics approval NBB-1037/2018), in the Netherlands Institute of Neuroscience, Amsterdam, the Netherlands. The use of the brain from which the cortical Broca sample was obtained was approved by the ethics committee of the medical faculty of the Heinrich Heine University Düsseldorf, Germany (approval #2023-2632).

2.3. Basis implementation and signal reconstruction

In general, a measurement basis is defined as any binary, orthogonal matrix Φ, whose row vectors Φ_i are mutually orthogonal, i.e., $\Phi_i \cdot \Phi_j = \delta_{i,j}$, where $\delta_{i,j}$ denotes the Kronecker delta. In this work, two such bases were considered: the canonical basis and the Hadamard basis. Both can be represented as $N \times N$ matrices, where each row vector corresponds to one angular illumination step of the source. For this purpose, the illumination ring is divided into N equally-sized angular segments. During the measurement routine, the row vectors of the matrix Φ are sequentially applied to define which angular segments of the illumination source are activated for each measurement step.

Biomedical Optics EXPRESS

The acquired signal of SPI is a projection of the measurement vector x by the measurement basis Φ yielding the acquired data vector $y = \Phi \cdot x$ [16] for each pixel in the image. The measurement vector of the signal can be reconstructed by inverting the equation:

$$x = \Phi^{-1} \cdot y \,. \tag{2}$$

Note that this transformation is applied to each signal that is acquired in one pixel, resulting in a data shape of $[3600, 5600, N]$ (in this case: $N = 16, 32, 64$). The code for creating the illumination patterns and performing the Hadamard reconstruction, which is applied to the Hadamard data as first preprocessing step, is provided in Section 1 of the Supplement 1. Supplement 1 Fig. S1 compares the originally acquired Hadamard data without the application of the inverse Hadamard transform to the canonical data.

2.3.1. Canonical basis

The canonical basis is the simplest possible measurement basis and is represented by the identity matrix $I(N)$. The dimensionality N determines the number of angular elements, and thus the angular resolution of the measurement. Figure 1(C) illustrates the first three steps of the canonical basis $I(16)$, where only a single angular segment is activated per measurement.

This approach, currently used for angular ComSLI measurements, results in a relatively low illumination intensity per step, as only one out of N segments is active at any given time. Consequently, the light intensity per measurement is reduced to I_0/N, where I_0 denotes the total illumination intensity of the system.

2.3.2. Hadamard basis

The Hadamard basis is commonly used in SPI due to its ability to activate at least 50% of the optical elements in each measurement step, thus utilizing a larger fraction of the available light [16,18]. A Hadamard matrix H satisfies the property $HH^T = H^2 = NI$, and consists of binary values ± 1. In practical implementations, the Hadamard matrix is decomposed into its positive and negative binary components: $H = H^+ - H^-$, so that $H^+ = (H + 1)/2$ and $H^- = -(H - 1)/2$ both containing only binary values (0 and 1). Measurements are then performed separately for the positive and negative components, yielding signals y^+ and y^-, respectively. The final signal is computed as: $y = y^+ - y^-$ and the image is then reconstructed via $x = Hy = HHy = Ny$. However, this double sampling of both H^+ and H^- increases acquisition time and introduces additional noise. An alternative approach samples only the positive part, with the original signal reconstructed using: $y = 2y^+ - y_0^+$ where y_0^+ is the measurement vector corresponding to a pattern in which all angular segments are active [26]. This approach improves SNR by eliminating the noise obtained during sampling the negative basis components. Figure 1(D) shows the first three Hadamard patterns used in the measurement process, as they are displayed on the LED display.

The code for the pattern generation and Hadamard transform of the signal is presented in the Supplement 1. To apply the Hadamard basis in this context, it is assumed that the total light intensity from multiple active segments is the sum of their individual intensities, i.e., $I_{\text{tot}} = \sum_i I_i$. This assumption holds under the condition of incoherent scattering, meaning that either multiple scattering events do not occur or are rare enough to be considered negligible. This assumption is crucial for the linear superposition of scattering signals and the validity of the Hadamard-based reconstruction.

2.4. Normalization of the acquired data

The setup was calibrated to compensate for variations in illumination and scattering paths by introducing an opal-glass diffuser (Edmund Optics #46-168) that produces a uniform scattering pattern. For each illumination pattern, $n = 100$ images were recorded, and the average intensity

Biomedical Optics EXPRESS

was calculated at each pixel (x, y). This procedure was repeated for all illumination patterns i of the Hadamard and canonical bases across all basis sizes ($N = 16, 32, 64$). Under these conditions, the angular scattering profile approximates a constant line corresponding to uniform scattering.

Finally, the measured intensities I_{meas} were normalized by the corresponding calibration values I_{ref} to quantify deviations from the uniform-scattering case:

$$I(x, y, i) = I_{\text{meas}}(x, y, i)/I_{\text{ref}}(x, y, i) \; . \tag{3}$$

2.5. Fiber orientation reconstruction

For each illumination angle, the transmitted (scattered) light intensity is captured by the camera, producing an angular scattering profile. Light scatters predominantly perpendicular to in-plane fiber bundles, resulting in paired peaks in the azimuthal intensity profile [10] (see Fig. 1(A)). Hence, the in-plane orientation is calculated from the angular mid-position of the peak pair.

Orientation estimation was performed using the SLIX software [27], which applies a peak detection algorithm similar to SciPy's *find_peaks* method, identifying significant peaks based on their prominence. Single peaks are interpreted as out-of-plane fibers with the position of the peak determining the in-plane fiber orientation φ. Pairs of peaks are matched if their angular separation falls within a window of $180° \pm 35°$, from which the local fiber orientation is derived. If more than two peaks are present in the profile, SLIX can resolve multiple directions by identifying all valid peak pairs within the signal, for up to three distinct fiber orientations φ_{1-3}. Full software documentation is available in [27].

Before applying the SLIX algorithm, the scattering profile for each pixel was normalized using $I = I/\max(I)$. For canonical angular sampling, a peak prominence threshold of 8% was applied, while for Hadamard-based measurements a higher threshold of 20% was used to account for differences in baseline intensity and signal characteristics.

3. Results

3.1. PLA sample

To compare the performance of the Hadamard and canonical bases, first it is verified that both measurement schemes yield consistent results. For this purpose, a scattering phantom made from PLA is used. Figure 2(A) shows the first entry of the reconstructed in-plane orientations of the PLA sample for $N = 32$. The displayed orientation direction is encoded in color as defined by the color wheel and follows the visual orientation of the PLA structure very clearly. Four regions of interest (ROIs) were selected (A1–A4, highlighted as white squares) to compare the angular scattering profiles derived from the canonical and Hadamard bases. ROIs A1 and A3 contain single fibers, while A2 and A4 include fiber crossings.

Insets B/C 1-4 in Fig. 2 present the reconstructed in-plane orientations of the canonical and Hadamard basis with $N = 32$ corresponding to ROI 1-4, respectively. In each pixel, small white lines indicate the two principal orientations that are found with the SLIX tool, while the large double-headed arrows indicate the directions of the PLA fibers. Overall, both bases yield the same reconstructed orientations. However, in the case of the crossing fibers in inset B/C2 and B/C4, the Hadamard basis features shifts of 90° at the borders of the PLA fibers, because only a single peak is detected. This phenomenon is further explored in the discussion of Fig. 8.

Insets D1-D4 in Fig. 2 display the angular scattering patterns for the canonical (black) and Hadamard (red) bases for $N = [16, 32, 64]$ angular segments. Each line profile is averaged over a 10×10 pixel region and normalized to the same total light intensity. Different offsets were applied to separate the profiles of different basis elements for better legibility. The normalized angular scattering profiles are presented in Supplement 1 Fig. S2.

As expected, increasing the number of angular segments N improves angular resolution and allows better separation of multiple scattering peaks. Overall, the angular profiles obtained from

Biomedical Optics EXPRESS

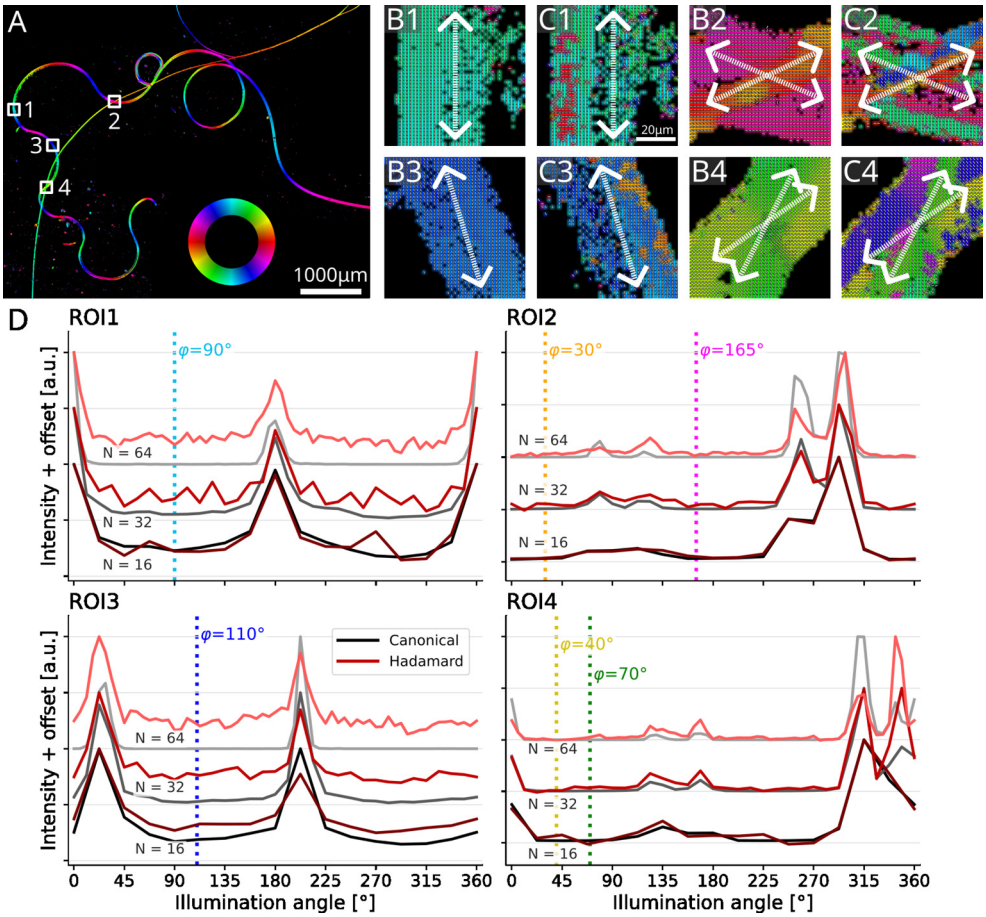

Fig. 2. Comparison of fiber orientations and scattering profiles for a PLA sample. A: First entry of the reconstructed in-plane orientations for $N = 32$ with four selected ROIs, indicated by white squares. The orientation is indicated by the color wheel. B/C 1-4 show zoomed-in views of the ROIs for the canonical (B) and Hadamard bases (C), respectively. Small white lines show the orientations for each pixel, while the large double-headed arrows indicate the direction of the PLA structure. D1-4: Angular scattering profiles of the four selected ROIs for the canonical (black) and Hadamard (red) bases for $N = [16, 32, 64]$ basis elements. For better legibility, the profiles for different N are shown with a different offset. The normalized angular scattering profiles can be found in Supplement 1 Fig. S2. Vertical lines indicate the reconstructed fiber orientations for $N = 32$. A high resolution image is provided as Visualization 1.

Biomedical Optics EXPRESS

both bases exhibit high similarity – particularly in peak position – regardless of whether the underlying structure corresponds to a single fiber (D1, D3) or a crossing (D2, D4). Notably, while the peak positions align well, the Hadamard basis often shows a higher, noise contaminated signal baseline, especially for larger values of N (i.e., $N = 32$ and $N = 64$), likely due to contributions from surrounding pixel intensities resulting from background scattering. However, peak prominence for $N = 64$ is consistently larger for the Hadamard basis.

Figure 3(A) shows the distribution of peak widths defined as the Full Width at Half Maximum (FWHM) determined by SLIX for all significant peaks for the canonical (black) and Hadamard (red) bases with $N = 16, 32$, and 64 basis elements. The distributions are shown as box plots on the left and violin plots on the right. The median values are similar for the canonical and Hadamard bases for all three values of N. However, the Hadamard basis shows a broader distribution, with more small and large peak widths than the canonical basis. For $N = 16$ and $N = 64$, the canonical basis yields peak widths that are 1.7° and 5.9° smaller, respectively. For $N = 32$, the Hadamard basis yields a peak width that is 0.9° smaller. Welch's t-test yielded p-values reported as 0 for all cases, indicating statistical significance.

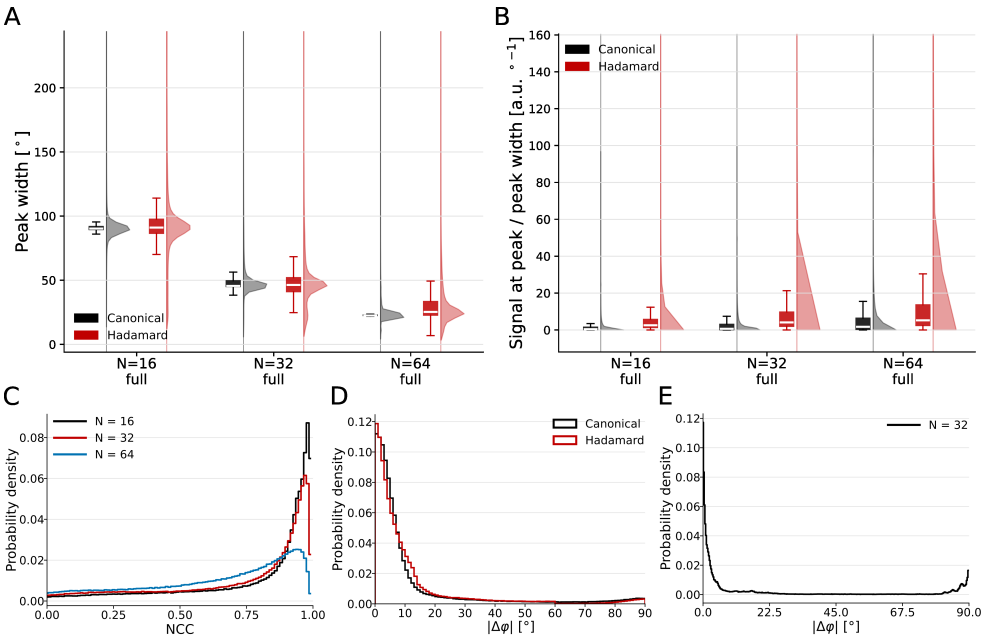

Fig. 3. Statistical signal analysis of the PLA sample. A: Box (left) and violin (right) plots of the peak-width distribution for $N = 16, 32$, and 64 basis elements for the canonical (black) and Hadamard (red) bases. B: Box (left) and violin (right) plots of the signal at the peak divided by the peak width for different values of N and both bases. C: Histogram of the NCC between canonical and Hadamard signals for $N = 16$ (black), 32 (red), and 64 (blue). D: Histogram of the orientation differences between the canonical and Hadamard bases and a structure tensor analysis. E: Histogram of the orientation differences between the canonical and Hadamard bases for $N = 32$.

Because the angular scattering profiles contain multiple peaks, a typical SNR definition (i.e., SNR = mean/standard deviation) does not provide usable information. The standard deviation increases when more prominent peaks are recorded in a scattering profile. Instead, the Signal to Width Ratio (SWR) evaluated at each peak is more appropriate [28]:

$$\mathrm{SWR} = \frac{S_{\mathrm{peak}} - S_{\mathrm{baseline}}}{\mathrm{FWHM}}. \tag{4}$$

Biomedical Optics EXPRESS

This metric directly correlates with the peak-finding performance of SLIX because more prominent and sharper peaks are easier to detect. The resulting distribution is presented in Fig. 3(B) for $N = 16, 32$ and 64 basis elements, in the same format as Fig. 3(A). In all cases, the Hadamard basis yields a broader distribution, independent of N. The median SWR increases with N, from 9 deg^{-1} to 15 deg^{-1} and 26 deg^{-1}. Welch's t-test yielded significant differences for all N, with p-values reported as 0.

To quantify the similarity between the two measurement schemes, the Normalized Cross Correlation (NCC) is used. This metric accounts for baseline differences and background noise, and is defined as:

$$\text{NCC}(A, B)_N = \frac{\sum_{i=1}^{N}(A_i - \bar{A})(B_i - \bar{B})}{\sqrt{\sum_{i=1}^{N}(A_i - \bar{A})^2} \cdot \sqrt{\sum_{i=1}^{N}(B_i - \bar{B})^2}},$$

where A and B are the scattering profiles from the canonical and Hadamard bases for a fixed N, respectively, $\bar{x}$ denotes the mean, and i indexes the angular segments.

Table 1 presents the NCC values for each ROI and for different values of N. All selected ROIs exhibit NCC values above 0.8, indicating strong agreement between the two sampling approaches.

Table 1. Normalized Cross Correlation for the ROIs 1-4 of Fig. 2 A1-4 and the full PLA sample for $N = 16, 32, 64$ basis elements.

N	ROI 1	ROI 2	ROI 3	ROI 4	Full sample
16	0.958	0.996	0.966	0.990	0.910 ± 0.256
32	0.922	0.980	0.958	0.924	0.860 ± 0.273
64	0.880	0.920	0.829	0.633	0.728 ± 0.273

Additionally, a global analysis was performed across the full PLA sample. A threshold mask was applied to isolate the PLA region, and NCC was computed pixel-wise across the image. For over 300,000 pixels, NCC values range between 0.5 and 0.9. A slight decrease in NCC with increasing N is observed. A histogram of the NCC distribution for $N = 32$ which is centered at NCC = 0.9 is shown in Fig. 3(C). The Supplement 1 Fig. S5 shows NCC maps for $N = 16, 32$ and 64 with the corresponding histograms.

A Structure Tensor Analysis (STA) [29] was performed to compare the directions obtained from the Hadamard and canonical bases with the structural directions of the sample. Although STA does not provide a direct angular ground-truth error and should therefore be considered an approximate structural reference, its directional estimates are expected to be more precise for the PLA sample than for brain tissue. This is because the PLA structures have clearly defined borders and a homogeneous macroscopic orientation, whereas brain tissue contains low-contrast regions, crossings, and heterogeneous fiber architectures. Reported STA uncertainties in brain tissue are on the order of $6° - 11°$ depending on the tissue region [30]. For the PLA sample, the expected uncertainty is therefore assumed to be smaller than these values. Overall, both sampling strategies show good agreement with the STA directions, with differences on the order of 10°, which corresponds to the angular resolution of ComSLI for $N = 32$ of $\Delta\phi = 11.25°$.

To quantitatively assess the similarity of the orientation reconstruction of the two sampling strategies, the minimal angular differences between the orientation maps were calculated for all three orientation vector components. The resulting distribution is shown as a histogram in Fig. 3(E). Two distinct peaks are observed: a dominant peak near 0°, and a smaller peak centered around 90°. The latter arises from the 90° orientation shift at the borders of the PLA sample. Overall, a median angular difference of 0.58° and a mean difference of $3.83 \pm 4.39°$ indicate high concordance between the reconstructed orientations of the two bases.

Biomedical Optics EXPRESS

3.2. Tissue samples

3.2.1. Human optic tract sample

To create a controlled biological sample with known fiber crossings, two sections of a human optic tract, each 30 µm thick, were stacked at a crossing angle of approximately 60°. The optic tract can be considered as quasi-parallel nerve fiber bundles, making it well-suited for artificially generating crossing fiber regions. In previous publications [7,21,24,31], the sample has successfully been used as model system to assess the reconstruction of crossing fiber orientations. Figure 4(A) shows the reconstructed first in-plane orientation entry of the prepared sample in the crossing region for $N = 32$. One section of the optic tract extends from the bottom left to the top right (indicated by three, small dotted lines), while the other section, placed on top, runs from the top left to the bottom right (indicated by two larger dashed lines). Four ROIs were selected for analysis: ROI 1 represents fibers from the top strand, ROI 2 from the bottom strand, ROIs 3 and 4 are located in the crossing region.

The reconstructed fiber orientations of the two crossing optic tract sections are shown in Fig. 4(A). The two distinct fiber bundles of the optic tract sample are clearly distinguishable: the top strand consistently appears in violet, indicating an orientation of approximately +155°, while the bottom strand appears in yellow, corresponding to an orientation of approximately +35°. These values are in agreement with the observed intersection angle of ~ 60°.

Subfigures 4(B) and (C) illustrate the distribution of the reconstructed fiber orientations for kernels of (32×32) pixels at the intersection of the upper and lower strands of the optic tract sections, obtained using the canonical (B) and Hadamard (C) bases, respectively. Four distinct regions can be identified: (i) the upper strand only, (ii) the lower strand only, (iii) the crossing region, and (iv) the tissue boundary and background.

The vector lines are color-coded according to their orientation, following the color wheel shown in Fig. 4(A). Both vector distribution maps exhibit strong visual agreement, particularly in regions (i) and (ii), where only a single fiber strand is present. In the crossing region (iii), the reconstructed orientations are likewise highly consistent between both bases, revealing crossing angles of approximately $45 - 60°$. In addition, both reconstructions show localized crossing angles of approximately 80°, indicated by blue vector components, which likely reflect local deviations of individual fibers from the macroscopic orientations of the optic tract sections.

The canonical basis yields a more continuous distribution of orientation vectors, as indicated by the presence of red components, whereas the Hadamard basis produces a sharper separation between crossing orientations.

In region (iv) (tissue boundary and background), the reconstructed orientations are predominantly orthogonal to the tissue structures. This behavior arises from SLIX assigning the orientation along the direction of a single peak, consistent with the observations in Fig. 2. Nevertheless, the Hadamard basis results in a higher proportion of vectors that align with the macroscopic anatomical features of the sample compared to the canonical basis, especially at the top strand (i).

Figure 4 D1-4 presents the angular scattering profiles for the canonical (black) and Hadamard (red) bases, for $N = 16, 32, 64$ angular illumination steps. The results are consistent with those obtained from the PLA sample (Fig. 2). Both measurement bases produce highly similar scattering profiles, while the Hadamard basis generally exhibits a slightly higher baseline. ROIs 1 and 2, which contain primarily single fiber orientations, show two distinct peaks corresponding to the expected angular scattering directions. Notably, the Hadamard-based measurements produce slightly narrower peaks with lower FWHM compared to the canonical basis, indicating improved angular resolution. In ROIs 3 and 4, where fiber crossings occur, four distinct peaks are visible in the angular profiles. In the canonical basis, peak overlap is more pronounced due to the broader FWHM, particularly in ROI 3, where overlapping peaks appear as one central peak flanked by

Biomedical Optics EXPRESS

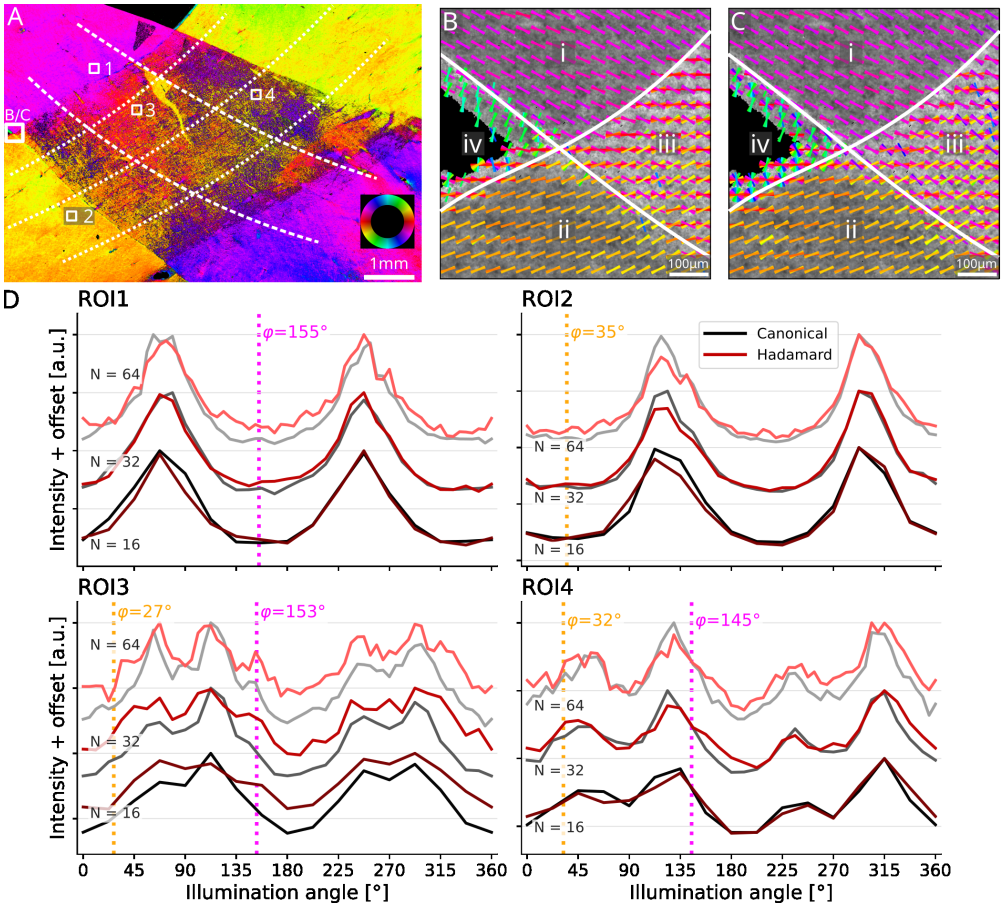

Fig. 4. Comparison of fiber orientations and scattering profiles of two crossing layers of the human optic tract. A: First entry of the reconstructed in-plane fiber orientations for $N = 32$ with four selected ROIs, indicated by white squares. The orientation is indicated by the color wheel. B and C show the fiber orientation map for the white ROI at the left image border for the canonical (B) and Hadamard bases (C), respectively. Fiber orientations are displayed on top of each other as colored lines for kernels of 32×32 pixels. White lines indicate the separation between four regions: (i) upper layer, (ii) bottom layer, (iii) crossing region, (iv) background and tissue border. The background shows an averaged intensity image that provides structural context. D1-4: Angular scattering profiles for the four selected ROIs for the canonical (black) and Hadamard (red) bases for $N = [16, 32, 64]$ basis elements. For better legibility, the profiles for different N are shown with a different offset. The normalized angular scattering profiles can be found in Supplement 1 Fig. S3. Vertical dashed lines indicate the reconstructed fiber orientations for $N = 32$. A high resolution image is provided as Visualization 2.

Biomedical Optics EXPRESS

smaller side peaks. In contrast, the Hadamard basis allows a clear separation of the individual peaks, enhancing the visibility of distinct fiber orientations.

To further evaluate this effect, Fig. 5(A) compares the peak widths for different values of N and for larger predefined regions, namely the full sample, the crossing region, and the non-crossing region. The distributions are shown for the canonical (black) and Hadamard (red) bases as box plots on the left and violin plots on the right. For $N = 16$, the canonical basis has slightly smaller peak widths. With increasing N, the Hadamard basis yields lower peak widths, as shown in Table 2. The difference is largest in the crossing region. In all cases, the difference is significant based on a Welch's t-test with p-values reported as 0.

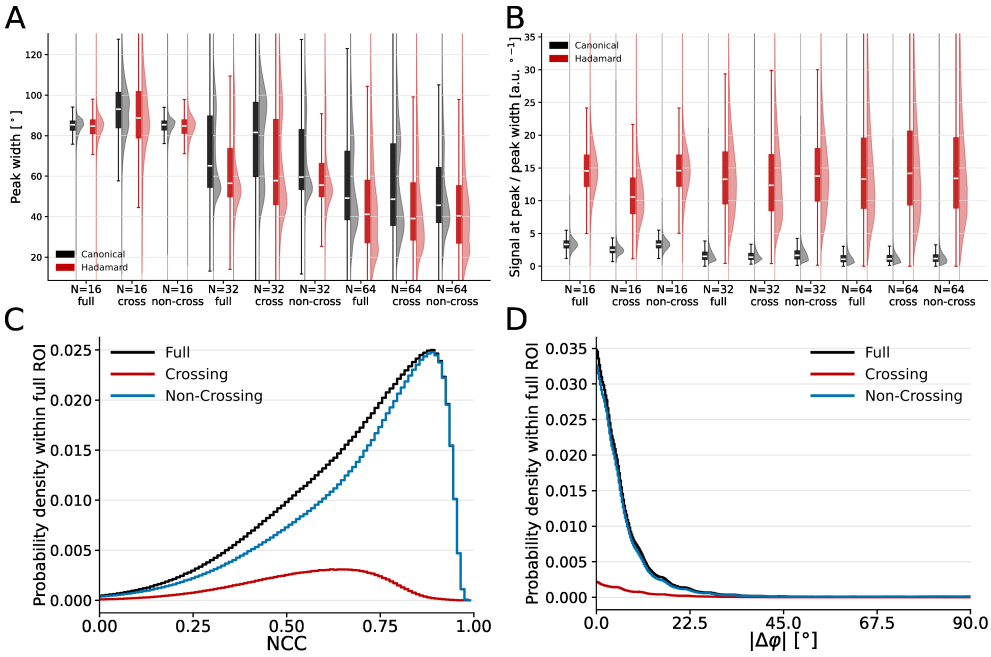

Fig. 5. Statistical signal analysis of the human optic tract sample. A: Box (left) and violin (right) plots of the peak-width distribution for $N = 16, 32$, and 64 basis elements for the canonical (black) and Hadamard (red) bases. B: Box (left) and violin (right) plots of the signal at the peak divided by the peak width for different values of N and both bases. C: Histogram of the NCC between canonical and Hadamard signals for the full sample (black), crossing areas (red), and non-crossing areas (blue). D: Histogram of the orientation differences between the canonical and Hadamard bases for the full sample (black), crossing areas (red), and non-crossing areas (blue).

Table 2. Mean difference of the peak width (ΔFHWM = $FWHM_N^{can} - FWHM_N^{Had}$) for the crossing and non-crossing areas, and the full optic tract sample (in degrees).

N	Crossing region	No crossings	Full sample
16	3.36	1.39	1.65
32	-2.64	-0.76	-1.62
64	-10.24	-3.83	-4.84

Biomedical Optics EXPRESS

Figure 5(B) shows the distribution of the SWR, defined in Eq. (4), for the different regions and values of N in the same format. As in Fig. 5(A), the Hadamard basis shows a broader distribution. It is also significantly larger than for the canonical sampling basis (p-values reported as 0), with a mean difference of at least 10 in SWR units. This difference is independent of the observed region.

Table 3 presents the NCC values for each ROI, as well as average NCC values for the full image, the crossing region (Cr), and the non-crossing (NCr) region. The selected ROIs show strong agreement between the canonical and Hadamard measurements, with NCC values above 0.8. ROIs 1 and 2, corresponding to regions with a single dominant fiber orientation, yield slightly higher NCC values (>0.94) compared to ROIs 3 and 4 in the crossing region (approximately 0.80).

Table 3. Normalized Cross Correlation for the ROIs 1-4 of Fig. 4, the crossing and non-crossing areas, and the full optic tract sample.

N	ROI 1	ROI 2	ROI 3	ROI 4	Crossing region	No crossings	Full sample
16	0.946	0.989	0.860	0.925	0.684± 0.179	0.833 ± 0.179	0.813 ± 0.185
32	0.972	0.988	0.848	0.885	0.579 ± 0.176	0.758 ± 0.194	0.731 ± 0.199
64	0.968	0.982	0.874	0.894	0.479 ± 0.168	0.666 ± 0.202	0.637 ± 0.205

On a broader scale, the crossing region exhibits NCC values around 0.1 lower than the non-crossing region, likely due to the more complex angular structure. Nevertheless, the NCC remains in the range of $0.5 - 0.7$ across both the crossing regions and the full image, confirming a strong overall similarity between the two sampling schemes even in complex tissue configurations. The histogram in Fig. 5(C) confirms this behavior. Supplement 1 Fig. S6 shows NCC maps for $N = 16, 32$ and 64 with the corresponding histograms. This suggests that in complex tissue regions, the SLIX algorithm identifies different peak pairs in the scattering profiles depending on the used sampling basis.

Figure 5(D) shows the distribution of the minimal angle differences for the entire image (black), the crossing region (Cr, red), and the non-crossing regions (NCr, blue). All histograms exhibit a peak around 0°, indicating overall good agreement between the orientations reconstructed from both bases. Since the sample does not contain large structural elements, edge effects that typically lead to deviations greater than 80° are not observed. The angular difference in the full image and non-crossing areas average at $0.78 \pm 1.82°$ and $0.72 \pm 1.62°$ ($N = 10^7$ pixels), whereas the crossing region exhibits a broader distribution with an average of about $1.62 \pm 3.33°$ ($N = 8 \cdot 10^5$ pixels).

3.2.2. Human cortex sample

Figure 6(A) shows the first entry of the reconstructed in-plane orientation map of a 60 µm-thick human brain section located at the interface between major fiber pathways and the cortex within a sulcus of the Broca area. An overview of the sample is shown in Supplement 1 Fig. S8. From the bottom left to the top right corner the sulcus is encompassed by white matter (WM), which is built of densely packed fiber pathways occasionally projecting into the adjacent gray matter (GM). The border between white and gray matter is marked by a dashed white line. The gray matter consists of neurons and smaller nerve fibers responsible for local connectivity between cells and with white matter structures. Due to its heterogeneous composition, the gray matter scatters light more diffusely, resulting in attenuated signals and more homogeneous scattering patterns. This makes resolving fiber crossings in gray matter particularly challenging, yet it is precisely these fine-scale connections that are of primary interest for understanding neuronal interconnectivity. Nonetheless, the grid-like structure of the cortical nerve fibers is clearly visible

Biomedical Optics EXPRESS

in the direction maps and highlighted by white lines. Direction maps similar to Figs. 6(B) and (C) were used as reference for the labeling.

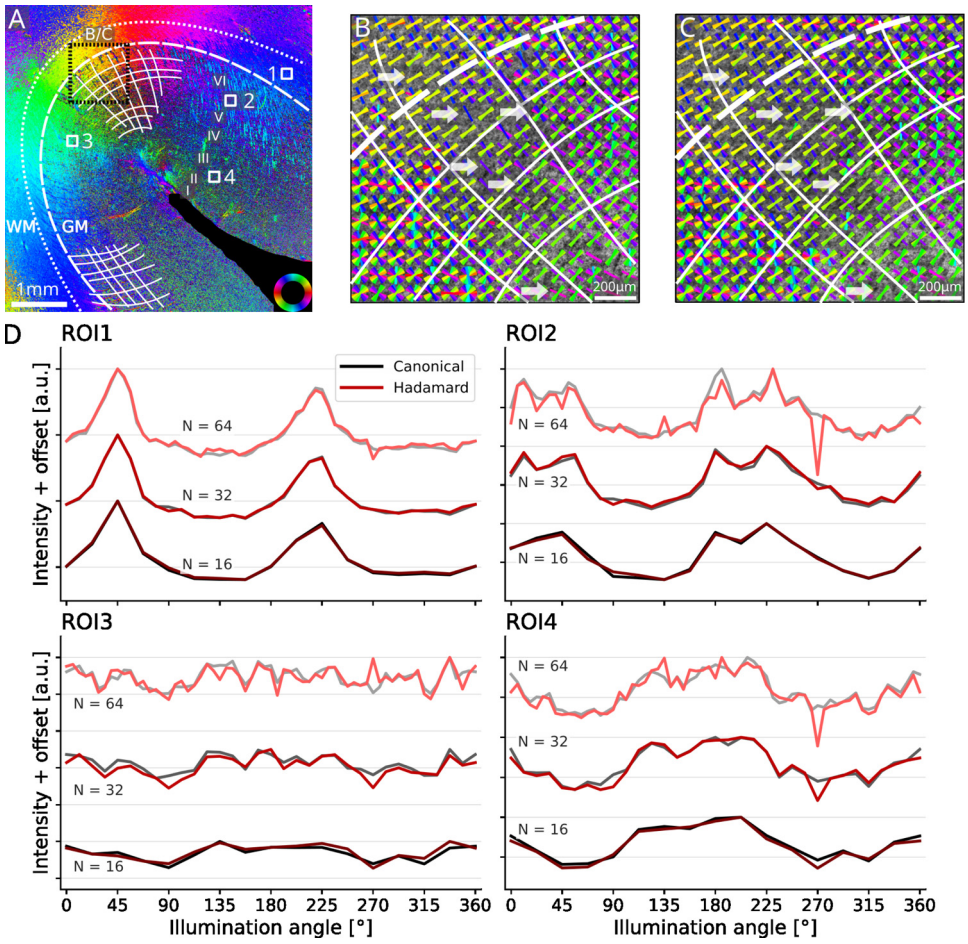

Fig. 6. Comparison of fiber orientations and scattering profiles for the human cortical brain tissue sample. A: First entry of the reconstructed in-plane fiber orientations for $N = 32$ with four selected ROIs, indicated by white squares. The orientation is indicated by the color wheel. The border between white (WM) and gray matter (GM) is indicated by a white dashed line. Fiber pathways are indicated by white lines. I-VI: approximate locations of cortical layers. B and C show the fiber orientation distribution for the black-dashed ROI at the WM-GM border for the canonical (B) and Hadamard bases (C), respectively. Fiber orientations are displayed on top of each other as colored lines for kernels of 32×32 pixels. White lines indicate dominant fiber orientations of the cortical fiber architecture. Differences between the two vector maps are indicated by white arrows. The background shows an averaged scattered light intensity image that provides structural context. D1-4: Angular scattering profiles for the four selected ROIs for the canonical (black) and Hadamard (red) bases for $N = [16, 32, 64]$ basis elements. For better legibility, the profiles for different N are shown with a different offset. The normalized angular scattering profiles can be found in Supplement 1 Fig. S4. A high resolution image is provided as Visualization 3.

The first entry of the direction map reconstructed using the Hadamard basis with $N = 32$ angular measurements is shown in Fig. 6(A). The white matter appears significantly brighter than the gray matter due to the higher density of aligned fibers. The fiber trajectory within the

Biomedical Optics EXPRESS

white matter can be followed from the lower left to the upper right of the image (indicated by a white, dotted line). Along this path, the orientation gradually changes from approximately +110° (blue) to 90° (cyan) and further to +45° (yellow) when moving upward from the lower left, following the curvature of the sulcus. Subsequently, the orientation transitions through 0° (red) to approximately −70° (green) as the fibers approach the upper right image border. In contrast, the gray matter exhibits a comparatively uniform distribution of orientations.

These observations are consistent with previous studies [10]. Figures 6(B) and (C) depict the distribution of reconstructed fiber orientations for kernels of (32 × 32) pixels at the WM–GM border (thick white dashed line), obtained using the canonical (B) and Hadamard (C) bases, respectively. White lines indicate the dominant cortical fiber architecture, derived from the principal components of the vector distribution maps. The vector lines are color-coded according to their orientation, following the color wheel shown in Fig. 6(A).

Both vector maps exhibit strong agreement in the overall orientation distribution, particularly within the white matter region, which is predominantly characterized by yellow vector components. In the gray matter, the orientations largely follow the white matter direction, preserving the yellow components while exhibiting an increased fraction of more heterogeneous orientations. Differences in both vector maps are indicated by white arrows. The gray matter is dominated by blue, purple, and green vector components. Whereas the green and orange components represent only minor deviations from the primary white matter orientation and can be attributed to local fiber variations, the blue components indicate an approximately 90° shift relative to the white matter orientation. This mesh-like orthogonal reorientation is a hallmark of the documented cortical fiber architecture [22]. The more randomized orientation components at the bottom left and top right are likely associated with local structural variability and noise due to reduced fiber density.

Both the canonical and Hadamard bases reproduce the characteristic cortical myeloarchitecture. However, the Hadamard basis exhibits a higher proportion of yellow and green vector components, which are already present within the white matter region. Furthermore, the Hadamard reconstruction exhibits fewer randomized orientation components than the canonical basis, while still revealing a larger number of fiber crossings.

Four ROIs were selected for analysis, and their angular scattering profiles are shown in Fig. 6(D): ROI 1 is located within the white matter, ROIs 2 and 3 lie in the cortical layers IV to V, where single fibers form a mesh grid, indicated by white lines, ROI 4 originates from within the cortical layer II, containing predominantly neurons. Cortical layers I-VI were approximately labeled by evaluating the fiber orientation maps [32].

As in previous experiments, angular scattering profiles for the canonical and Hadamard bases are shown in black and red, respectively, for $N = 16, 32, 64$ angular steps.

The scattering profile for ROI 1 (Fig. 6 D1) shows high agreement between the two bases, similar to previous findings in Fig. 4. Peak positions align very well.

This general trend also holds for ROIs 2–4. However, as the angular resolution increases (i.e., $N = 64$), the Hadamard basis reveals a larger number of smaller peaks.

Table 4. Mean difference of the peak width (ΔFHWM = $FWHM_N^{can} - FWHM_N^{Had}$) for the white matter and gray matter areas, and the full cortex sample (in degrees).

N	White matter	Gray matter	Full sample
16	-0.58	-9.35	-5.58
32	-0.27	-5.25	-3.44
64	-0.88	-3.00	-2.63

Biomedical Optics EXPRESS

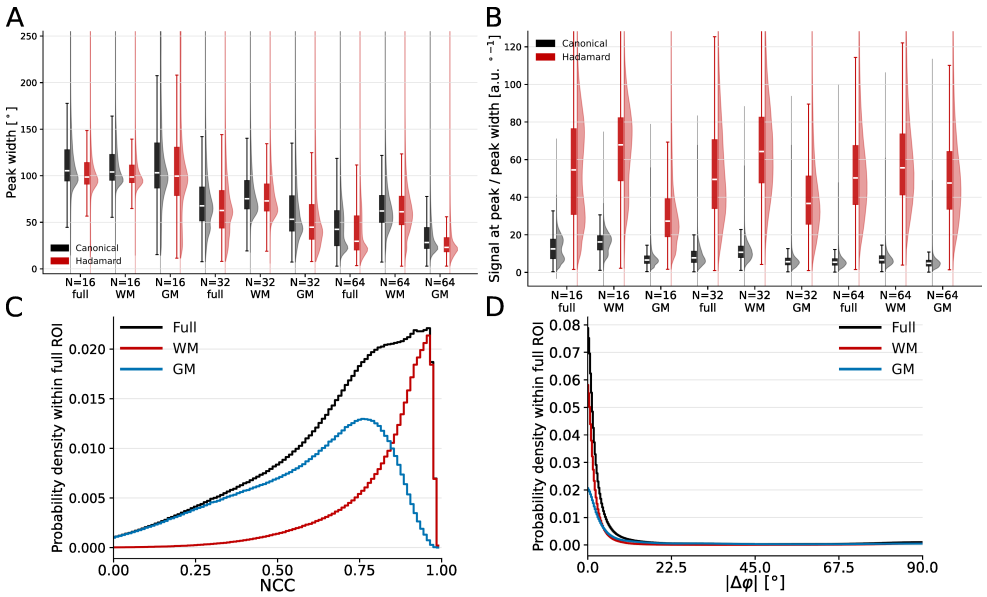

Fig. 7. Statistical signal analysis of the human cortex sample. A: Box (left) and violin (right) plots of the peak-width distribution for $N = 16, 32$, and 64 basis elements for the canonical (black) and Hadamard (red) bases. B: Box (left) and violin (right) plots of the signal at the peak divided by the peak width for different values of N and both bases. C and D: Histograms of the NCC and minimal angular difference for the canonical and Hadamard signals for $N = 32$, respectively. Full sample (black), WM: white matter (red), GM: gray matter (blue).

Figure 7(A) compares the peak widths for different values of N and for larger regions, namely the full sample, white matter (WM), and gray matter (GM). The distributions are shown for the canonical (black) and Hadamard (red) bases as box plots on the left and violin plots on the right. Independent of N and region, the Hadamard basis yields a lower median peak width, as indicated by the box plots. Moreover, the violin plots show that the Hadamard basis yields more small peak widths than the canonical basis. The mean difference in peak width is presented in Table 4. The difference is largest in the gray matter region. In all cases, the difference is significant based on a two-sided t-test with p-values reported as 0.

Figure 7(B) shows the distribution of the SWR, defined in Eq. (4), for the different regions and values of N in the same format. As in Fig. 7(A), the Hadamard basis shows a broader distribution. It is also significantly larger than the canonical sampling basis (p-values reported as 0), with a mean difference of at least $20\,\mathrm{deg}^{-1}$ for $N = 16$ and $40\,\mathrm{deg}^{-1}$ for $N = 32$ and 64. This difference is independent of the observed region.

Despite these differences in peak detail, NCC values between the two bases remain high, as shown in Table 5. NCC values range from 0.70 to 0.99 across the selected ROIs.

Table 5. Normalized Cross Correlation for the ROIs 1-4 of Fig. 6, the white and gray matter areas, and the full brain cortex sample.

N	ROI 1	ROI 2	ROI 3	ROI 4	White matter	Gray matter	Full sample
16	0.982	0.953	0.796	0.923	0.911 ± 0.148	0.749 ± 0.219	0.819 ± 0.212
32	0.985	0.951	0.753	0.901	0.875 ± 0.154	0.643 ± 0.221	0.738 ± 0.227
64	0.990	0.886	0.700	0.902	0.805 ± 0.182	0.522 ± 0.214	0.622 ± 0.238

Biomedical Optics EXPRESS

When evaluating the entire image (comprising about 10 million pixels (green channel only)), the NCC values again show a slight decrease with increasing N, consistent with the ROI observations. The Hadamard basis reveals additional peaks that are either blurred or absent in the canonical basis, leading to slight divergences in signal shape. Nevertheless, even at $N = 32$, the average NCC exceeds 0.8, indicating strong correlation between the two methods. The Supplement 1 Fig. S7 shows NCC maps for $N = 16, 32$ and 64 with the corresponding histograms.

To further evaluate structural differences, Gaussian mixture model segmentation is applied to separately mask white and gray matter regions. NCC values are then computed for each region independently. Across all values of N, the white matter consistently exhibits NCC values that are $0.15 - 0.2$ points higher than those in the gray matter, reflecting the increased complexity and lower SNR in the latter. The histogram in Fig. 6(F) clearly illustrates this separation, with the distributions of white matter (red line) and gray matter (blue line) showing distinct peaks.

The histogram in Fig. 7(D) shows the distributions of angular differences for the full image (black), white matter (red), and gray matter (blue). Similar to the results for the optic tracts (Fig. 4(D)), all distributions are centered around 0°, indicating that the majority of reconstructed directions agree across sampling methods. However, the gray matter shows a higher variance compared to the white matter, similar to the crossing region in the optic tract sample. These findings are consistent with the NCC values reported in Table 5, where the lower correlation in the gray matter is attributed to the Hadamard basis detecting more peaks in the scattering profiles. As a result, the SLIX algorithm identifies different peak pairs for orientation reconstruction in this region.

4. Discussion

Overall, sampling the angular illumination patterns using the Hadamard basis not only reproduces, but also outperforms those obtained using the established canonical basis for simple scattering structures. Because the Hadamard basis activates at least 50% of the illumination patterns at any given time, the effective light intensity during acquisition is increased by $0.5N$ compared to the canonical basis according to Eq. (1). For $N = 32$, this enables a tenfold reduction in exposure time (from 5.0 seconds to 0.5 seconds per image) without compromising data quality. This is relevant for high-throughput measurements of large biological tissue sections, which typically span an area of $10 \times 15\,\mathrm{cm}^2$. In the current setup, such an area requires 50×75 individual tile measurements, each with $N = 32$ images. Canonical basis sampling would require a measurement time of $50 \times 75 \times 32 \times 5\,\mathrm{s} = 166\,\mathrm{h}$, corresponding to approximately one week of continuous operation. Hadamard basis sampling would reduce this time to 16 h. The increased illumination and thus increased scattering intensity produces more sharply defined peaks, with an approximately 5° smaller FWHM for the Hadamard basis. This effect is more prominent in heterogeneous regions, including the crossing region of the optic tract sample and the gray matter of the cortex sample, as shown in Tables 2 and 4, respectively. The smaller peaks result in a significantly higher SWR by at least a factor of 10 and subsequently improve peak-finding performance in SLIX.

Analyzing angular scattering profiles in biological tissue remains challenging due to the absence of ground truth data and the inherent complexity and variability of biological structures.

For well-defined structures, such as the PLA sample shown in Fig. 2, both sampling methods yield highly similar results, as confirmed by the NCC values (Table 1) and the reconstructed direction maps (Fig. 2(B)/(C)). Decrease of the NCC value for larger N can be attributed to the reduced SNR at higher angular resolution of the canonical basis because the scattering power decreases with $1/N$. In regions where the PLA filament diameter is below 40 µm, the canonical and Hadamard results closely agree. However, in areas with larger diameters, edge effects can lead to directional shifts of approximately 90°, explaining some of the observed deviations.

Biomedical Optics EXPRESS

Larger structures tend to appear more homogeneously illuminated when using the canonical basis, primarily due to the longer acquisition times and lower light intensity. In contrast, the Hadamard reconstruction reveals more localized structural details, as the scattering signal is more pronounced at the structural boundaries (see Fig. 8). Since light is predominantly scattered at the interfaces between tissue and surrounding medium, the Hadamard basis enhances the spatial localization of scattering features, whereas the canonical images tend to appear more blurred.

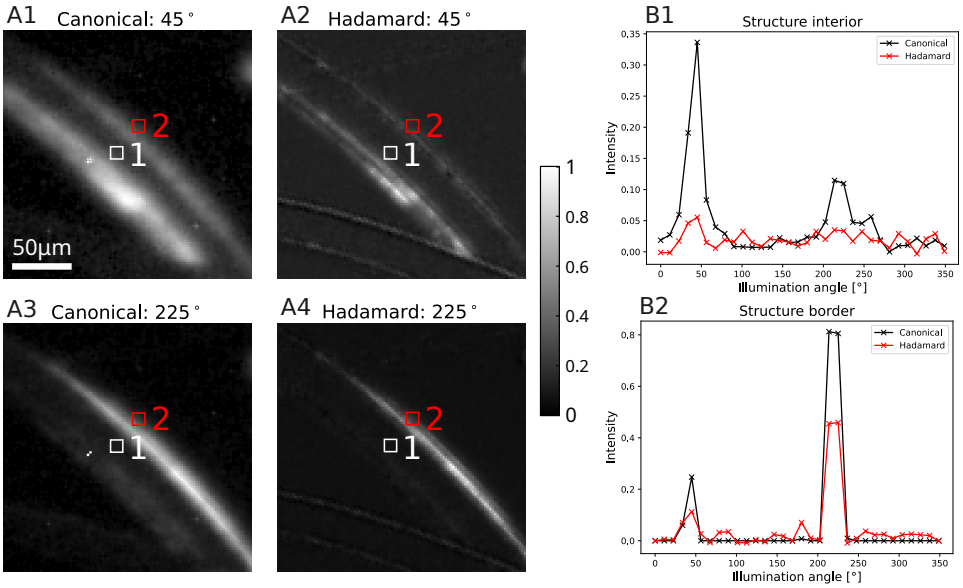

Fig. 8. Illumination difference for canonical basis (A1, A3) and reconstructed Hadamard basis (A2, A4) for $N = 32$. For particular illumination angles orthogonal to the structure orientation, the whole PLA structure is illuminated for the canonical basis, while the Hadamard basis only highlights the borders. Angular scattering profiles are shown for one region in the interior of the PLA structure (white square 1, B1) and at the structures border (red square, B2).

Additionally, the Hadamard basis produces more sharply defined and localized peaks with slightly narrower widths compared to those obtained with the canonical basis. This can be clearly observed in the ROI signals presented in Figs. 4 and 6. In particular, in cortical regions (e.g., Fig. 6 D2 and D3), the Hadamard basis reveals distinct peaks already at $N = 32$ angular steps, while similar features only emerge at $N = 64$ for the canonical basis. This supports the conclusion that the Hadamard basis achieves higher angular resolution.

This improved resolution is also reflected in the observed decrease in NCC values with increasing numbers of basis elements N, and thus finer angular resolution $\Delta\varphi = 360°/N$ (see Tables 1, 3, and 5). At lower angular resolutions, signals from both sampling methods align more closely, as finer structural variations are not resolved. Conversely, at higher resolutions, the Hadamard basis captures more detail, which may not be matched by the canonical basis, resulting in lower NCC values.

The data also show that NCC values calculated over large tissue regions are typically 0.1–0.2 points lower than those for localized ROIs. This is expected, as individual ROIs (spanning 10×10 pixels) exhibit more homogeneous structures, whereas larger areas encompass greater variability across millions of pixels.

Overall, the NCC values indicate strong agreement, as most NCC values are greater than 0.8 across the samples. Most NCC values are greater than 0.5, which still indicates good agreement

Biomedical Optics EXPRESS

between the two sampling strategies. Deviations between the two signals can be attributed to the increased illumination and resulting scattering intensity of the Hadamard basis, which yields more sharply defined scattering peaks and therefore higher angular resolution of the scattering profiles. This allows improved separation of potentially overlapping scattering peaks.

These differences in angular resolution help explaining the deviations in the direction maps between the Hadamard and canonical bases observed in Figs. 2 and 4. For the majority of pixels, the orientations reconstructed by both methods agree well, with differences <6.25°, which is half of the angular resolution for $N = 32$ basis elements. Regions with a single dominant fiber orientation, such as in the optic tract sample or the white matter of the cortex, show better agreement between the two methods. In contrast, regions of fiber crossings, exhibit larger deviations, as the Hadamard basis resolves more scattering peaks.

Table 6 shows the number of orientations detected by the canonical and Hadamard bases for the three samples. Except for the PLA sample in Fig. 2 where single peaks appear in the Hadamard basis due to the large sample dimensions, the Hadamard basis is able to detect consistently more double and triple orientations in a single pixel compared to the canonical basis, except for the non-crossing region of the optical tract sample in Fig. 4. Furthermore, the Hadamard basis resolves smaller minimal crossing angles in the tissue samples shown in Figs. 4 and 6, reaching values close to the angular resolution limit of 11.25°. This improvement is attributed to the higher SWR of the Hadamard basis, which enables more effective peak separation in the SLIX software.

Table 6. Number of orientations and minimal crossing angles reconstructed by the canonical (can) and Hadamard (Had) bases for each sample, where OT indicates the Optic Tract sample. Entries of φ_2 and φ_3 indicate double or triple crossings, respectively.

Sample	φ_1^{can}	φ_1^{Had}	φ_2^{can}	φ_2^{Had}	φ_3^{can}	φ_3^{Had}	$\Delta\varphi_{\text{min}}^{\text{can}}$	$\Delta\varphi_{\text{min}}^{\text{Had}}$
PLA	4.38 e5	4.52 e5	19.007	45,595	1.092	1,052	19.77°	19.59°
OT: Full	17.3 e6	17.5 e6	3.18 e6	3.31 e6	7.17 e5	7.18 e5	19.33°	10.74°
OT: Crossing	2.41 e6	2.64 e6	6.52 e5	9.05 e5	1.76 e5	1.99 e5	19.33°	10.74°
OT: Non-crossing	14.9 e6	14.8 e6	2.53 e6	2.41 e6	5.41 e5	5.19 e5	19.94°	12.28°
Cortex	9.07 e6	10.98 e6	1.62 e6	1.86 e6	4.85 e5	5.50 e5	18.70°	9.92°

This behavior is expected to be largely independent of sample thickness. Although the scattered-light intensity decreases with increasing sample thickness due to attenuation according to the Lambert-Beer law, this effect is independent of the sampling basis. The present study includes structures ranging from a few micrometers in diameter, as in the PLA sample, to biological tissue samples with thicknesses of 30 µm, corresponding to single strands of the optic tract sample, and 60 µm, corresponding to the crossing region of the optic tract sample and the human cortex sample. Across these different sample dimensions, no significant differences in the relative behavior of the two sampling approaches were observed.

Another important factor is the peak detection and orientation estimation performed by the SLIX software. Since SLIX offers limited tuning parameters and operates without a ground truth or formal signal model, it may incorrectly pair peaks in the Hadamard-derived scattering profiles – especially as these profiles often contain more peaks due to higher sensitivity. Moreover, too many peaks found in a single pixel might yield no primary direction in SLIX. This can lead to incorrect orientation estimations in regions with complex or noisy signals.

To address these limitations, future work should aim to develop a robust model for the angular scattering signal. Such a model would facilitate more accurate peak detection and orientation reconstruction, particularly for data acquired using the Hadamard basis.

One limitation of using the Hadamard basis is that the angular resolution is constrained to $N = 2^n$ steps due to the mathematical structure of the Hadamard matrix. Alternative sampling bases, such as randomized binary Gaussian matrices, enable the construction of $N \times N$ matrices

Biomedical Optics EXPRESS

with arbitrary dimensions. These are commonly used in compressive sensing applications [33,34]. However, for full-basis measurements, as done in this work, the signal reconstruction requires inverting the measurement basis, which might lead to rounding errors, which is not the case for the Hadamard basis. In future work, compressive sensing could be leveraged to reduce the total number of angular measurements required, thereby decreasing the data acquisition time while preserving essential information from the scattering profiles [35,36].

Finally, the successful application of Hadamard basis sampling also provides information about the scattering regime in the investigated samples. Hadamard reconstruction assumes that the measured signal is a linear superposition of the signals generated by the individual illumination segments [15]. In biological tissue, this assumption may be affected by multiple scattering, particularly in heterogeneous regions such as gray matter. However, the high agreement between the reconstructed Hadamard signals and the canonical measurements indicates that the linear superposition assumption is sufficiently fulfilled for the samples investigated here. This suggests that coherent or strongly nonlinear multiple-scattering contributions do not dominate the measured ComSLI signal under the present experimental conditions.

5. Conclusion

This work introduces structured light illumination to microscopic brain imaging and scatterometry, demonstrating that it not only reproduces, but also outperforms results comparable to conventional illumination techniques. By employing the Hadamard basis for angular sampling, the available illumination light is increased by a factor of $0.5N$, enabling a tenfold reduction in acquisition time when using an LED display as light source, reducing acquisition time for whole brain sections from days to hours. This increase of light intensity significantly increases the SWR at least by a factor of 6 and enhances the angular resolution of the scattering profiles. Furthermore, the higher SWR produces more prominent and sharply defined peaks, enabling consistent detection of multiple fiber orientations and smaller crossing angles within a single camera pixel when using the Hadamard basis, compared to the canonical basis.

As a result, the method enables finer structural resolution in heterogeneous and complex tissue regions with a low fiber density such as gray matter, offering potential for more detailed mapping of the brain's cortical fiber architecture – an area that remains a major challenge in current neuroscience research. Recent work suggests that the three-dimensional orientation of fiber structures can be inferred from angular scattering profiles [8], which may be more readily accessed using the Hadamard sampling approach. Furthermore, since the Hadamard reconstruction relies on the linearity assumption of incoherent scattering, the success of the method supports the conclusion that incoherent scattering is the dominant mechanism in the investigated brain tissue. Finally, the sampling of the Hadamard basis allows the application of compressive sensing of the angular scattering profiles in the future, further reducing acquisition time and data storage requirements.

Funding. Commissariat à l'Énergie Atomique et aux Énergies Alternatives (AIDAS); Deutsche Forschungsgemeinschaft (498596755); European Union (Horizon Program No. 101147319).

Acknowledgment. Thanks to Franca auf der Heiden who inspired the work with the motto of her PhD thesis: 'more light is more loot'. Special thanks to the lab team of INM-1 (Forschungszentrum Jülich GmbH, Germany) for preparing the brain samples, with particular appreciation to Anna Steffens, Phillip Schlömer, and Markus Cremer. The authors also thank Roxana Kooijmans for providing the optic tract sample. Generative AI was used for spelling and grammar correction.

Disclosures. The authors declare no conflict of interest.

Data availability. Data and scripts for the simulations can be found in the Supplement 1. Further data underlying the results presented in this article may be obtained from the corresponding author upon reasonable request.

Supplemental document. See Supplement 1 for supporting content.

Biomedical Optics EXPRESS

References

1. M. Axer and K. Amunts, "Scale matters: The nested human connectome," Science **378**(6619), 500–504 (2022).
2. I. Costantini, M. Axer, C. Magnain, *et al.*, "Editorial: The human brain multiscale imaging challenge," Front. Neuroanat. **16**, 1060405 (2022).
3. H. Al.Turkistani, F. Tashkandi, and Z. Mohammedsaleh, "Histological stains: A literature review and case study," Glob. J. Health Sci. **8**(3), 72–79 (2015).
4. B. Ghosh and K. Agarwal, "Viewing life without labels under optical microscopes," Commun. Biol. **6**(1), 559 (2023).
5. K. G. Schilling, V. Janve, Y. Gaos, *et al.*, "Histological validation of diffusion mri fiber orientation distributions and dispersion," NeuroImage **165**, 200–221 (2018).
6. M. Axer, D. Graessel, M. Kleiner, *et al.*, "High-resolution fiber tract reconstruction in the human brain by means of three-dimensional polarized light imaging," Front. Neuroinform. **5**, 34 (2011).
7. M. Menzel, J. A. Reuter, D. Gräßel, *et al.*, "Scattered light imaging: Resolving the substructure of nerve fiber crossings in whole brain sections with micrometer resolution," NeuroImage **233**, 117952 (2021).
8. M. Vermeulen, P. van Altena, and R. Mak, "Computational scattered light imaging of 3D-nanofabricated fiber models for an enhanced reconstruction of fiber 3D-orientations and diameters in biological tissues," in *Optical Methods for Inspection, Characterization, and Imaging of Biomaterials VII*, vol. 13571 P. Ferraro, S. Grilli, and D. Psaltis, eds., International Society for Optics and Photonics (SPIE, 2025), p. 135712A.
9. E. Ameh, "A review of basic crystallography and X-ray diffraction applications," Int. J. Adv. Manuf. Technol. **105**(7-8), 3289–3302 (2019).
10. M. Georgiadis, F. auf der Heiden, H. Abbasi, *et al.*, "Micron-resolution fiber mapping in histology independent of sample preparation," Nat. Commun. **16**(1), 9572 (2025).
11. F. Auf der Heiden, M. Axer, K. Amunts, *et al.*, "Scattering polarimetry enables correlative nerve fiber imaging and multimodal analysis," Sci. Rep. **15**(1), 18493 (2025).
12. M. Menzel, D. Gräßel, I. Rajkovic, *et al.*, "Using light and X-ray scattering to untangle complex neuronal orientations and validate diffusion MRI," eLife **12**, e84024 (2023).
13. F.-C. Yeh, A. Irimia, D. C. de Almeida Bastos, *et al.*, "Tractography methods and findings in brain tumors and traumatic brain injury," NeuroImage **245**, 118651 (2021).
14. B. Jeurissen, M. Descoteaux, S. Mori, *et al.*, "Diffusion MRI fiber tractography of the brain," NMR Biomed. **32**(4), e3785 (2019).
15. M. Edgar, G. Gibson, and M. Padgett, "Principles and prospects for single-pixel imaging," Nat. Photonics **13**(1), 13–20 (2018).
16. Graham M. Gibson, S. D. Johnson, and M. J. Padgett, "Single-pixel imaging 12 years on: a review," Opt. Express **28**(19), 28190–28208 (2020).
17. S. L. Brunton and J. N. Kutz, *Data-driven Science and Engineering: Machine Learning, Dynamical Systems and Control* (Cambridge University Press, 2019).
18. D. Scheidt and P. A. Quinto-Su, "Comparison between Hadamard and canonical bases for in situ wavefront correction and the effect of ordering in compressive sensing," J. Opt. Soc. Am. A **40**(1), 45–52 (2023).
19. I. M. Vellekoop and A. P. Mosk, "Focusing coherent light through opaque strongly scattering media," Opt. Lett. **32**(16), 2309–2311 (2007).
20. D. Scheidt, A. V. Arzola, and P. A. Quinto-Su, "Shaping the angular spectrum of a Bessel beam to enhance light transfer through dynamic strongly scattering media," Opt. Lett. **48**(24), 6360–6363 (2023).
21. M. Menzel, M. Ritzkowski, J. A. Reuter, *et al.*, "Scatterometry measurements with scattered light imaging enable new insights into the nerve fiber architecture of the brain," Front. Neuroanat. **15**, 767223 (2021).
22. R. Nieuwenhuys, "The myeloarchitectonic studies on the human cerebral cortex of the vogt-vogt school, and their significance for the interpretation of functional neuroimaging data," Brain Struct. Funct. **218**(2), 303 (2012).
23. M. Downing, D. Baade, and P. Sinclaire, "CCD riddle: a) signal vs time: linear; b) signal vs variance: non-linear," in *High Energy, Optical, and Infrared Detectors for Astronomy II*, vol. 6276 D. A. Dorn and A. D. Holland, eds., International Society for Optics and Photonics (SPIE, 2006), p. 627609.
24. M. Menzel, M. Axer, H. De Raedt, *et al.*, "Toward a high-resolution reconstruction of 3D nerve fiber architectures and crossings in the brain using light scattering measurements and finite-difference time-domain simulations," Phys. Rev. X **10**, 021002 (2020).
25. M. Stacho, C. Herold, N. Rook, *et al.*, "A cortex-like canonical circuit in the avian forebrain," Science **369**(6511), eabc5534 (2020).
26. W. Daixuan, L. Jiawei, H. Guoqiang, *et al.*, "Imaging biological tissue with high-throughput single-pixel compressive holography," Nature Comm. **12**, 4712 (2021).
27. J. A. Reuter and M. Menzel, "SLIX: A Python package for fully automated evaluation of Scattered Light Imaging measurements on brain tissue," Journal of Open Source Software **5**(54), 2675 (2020).
28. J. Feng, Y. Liu, X. Chen, *et al.*, "Theoretical design of composite stratified nanohole arrays for high-figure-of-merit plasmonic hydrogen sensors," Chemosensors **13**(8), 309 (2025).
29. R. Rezakhaniha, A. Agianniotis, J. Schrauwen, *et al.*, "Experimental investigation of collagen waviness and orientation in the arterial adventitia using confocal laser scanning microscopy," Biomech. Model. Mechanobiol. **11**(3-4), 461–473 (2012).

Biomedical Optics EXPRESS

30. B. Gray, A. W. Smith, A. MacKenzie-Graham, *et al.*, "Validation of structure tensor analysis for orientation estimation in brain tissue microscopy," J. Neurosci. Methods **423**, 110539 (2025).
31. M. Menzel and S. F. Pereira, "Coherent Fourier scatterometry reveals nerve fiber crossings in the brain," Biomed. Opt. Express **11**(8), 4735–4758 (2020).
32. N. Palomero-Gallagher and K. Zilles, "Cortical layers: Cyto-, myelo-, receptor- and synaptic architecture in human cortical areas," NeuroImage **197**, 716–741 (2019).
33. M. F. Duarte, M. A. Davenport, D. Takhar, *et al.*, "Single-pixel imaging via compressive sampling," IEEE Signal Process. Mag. **25**(2), 83–91 (2008).
34. F. Auf der Heiden, "High-speed multi-modal scattering polarimetry for nerve fiber imaging," Ph.D. thesis, Bergische Universität Wuppertal (2025).
35. F. auf der Heiden, O. Münzer, and S. van Staalduine, "Towards high-speed computational scattered light imaging by introducing compressed sensing for optimized illumination," in *High-Speed Biomedical Imaging and Spectroscopy IX*, vol. 12853 K. K. Tsia and K. Goda, eds., International Society for Optics and Photonics (SPIE, 2024), p. 1285303.
36. D. Scheidt, "Phase conjugation to enhance transmission and focusing of light through turbid media," Ph.D. thesis, Universidad Nacional Autónoma de México (2024).